View metadata, citation and similar papers at core.ac.uk

brought to you by CORE

provided by VBN

Aalborg Universitet

AALBORG UNIVERSITY
DENMARK

Wide Frequency Band Active Damping Strategy for DFIG System High Frequency Resonance

Song, Yipeng; Blaabjerg, Frede

Published in:
I E E E Transactions on Energy Conversion

DOI (link to publication from Publisher):
10.1109/TEC.2016.2591779

Publication date:
2016

Document Version
Peer reviewed version

Link to publication from Aalborg University

Citation for published version (APA):
Song, Y., & Blaabjerg, F. (2016). Wide Frequency Band Active Damping Strategy for DFIG System High Frequency Resonance. I E E E Transactions on Energy Conversion, 31(4), 1665-1675. DOI: 10.1109/TEC.2016.2591779

General rights
Copyright and moral rights for the publications made accessible in the public portal are retained by the authors and/or other copyright owners and it is a condition of accessing publications that users recognise and abide by the legal requirements associated with these rights.

? Users may download and print one copy of any publication from the public portal for the purpose of private study or research.
? You may not further distribute the material or use it for any profit-making activity or commercial gain
? You may freely distribute the URL identifying the publication in the public portal ?

Take down policy
If you believe that this document breaches copyright please contact us at vbn@aub.aau.dk providing details, and we will remove access to the work immediately and investigate your claim.

Downloaded from vbn.aau.dk on: May 01, 2017

Wide Frequency Band Active Damping Strategy for DFIG System High Frequency Resonance

Yipeng Song *Member, IEEE*, Frede Blaabjerg, *Fellow, IEEE*

***Abstract* — As a popular renewable power generation solution, the Doubly Fed Induction Generator (DFIG) based wind power system may suffer from High Frequency Resonance (HFR) caused by the impedance interaction between the DFIG system and the parallel compensated weak network. A wide frequency band active damping strategy for DFIG system HFR, including a high-pass filter and a virtual resistance, is proposed in this paper. The advantages of this active damping strategy are, 1) no resonance frequency detection unit is required, thus the control complexity can be decreased; 2) no active damping parameters adjustment is needed within certain wide frequency band, thus the robustness of the proposed active damping strategy can be improved. The parameter design of the high-pass filter cutoff frequency and the virtual resistance are theoretically analyzed with the purpose of satisfactory active damping. A 7.5 kW down-scaled experimental setup is built up for the experimental validation of the proposed active damping method.**

***Index Terms* — DFIG system impedance; high frequency resonance active damping; high-pass filter; virtual resistance; parameters design.**

I. Introduction

The control technology of Doubly Fed Induction Generator (DFIG) based wind power generation system has been under increasing development for the past decades, and large scale commercial implementations of wind turbine are all around the world [1]. Improved control strategies for DFIG system under steady state unbalance [2], harmonic distortion [3]-[4], voltage disturbances [5], and low voltage fault [6] have been well investigated.

In order to utilize large scale wind power, more and more DFIG based wind turbine systems are connected to the offshore and distributed networks, which might be smaller scale weak networks with comparatively large network impedances. Consequently, the impedance interaction between the weak power network and the DFIG system may unfortunately produce both Sub- Synchronous Resonance (SSR) and High Frequency Resonance (HFR), and these resonances deserve serious consideration.

When radially connected to a series compensated network, the Sub- Synchronous Resonance (SSR) [7]-[14] may occur due to the impedance interaction between the DFIG system and the series compensated grid network. As a basis of analyzing the SSR, the DFIG system impedance modeling should be built up first. Ref. [7]-[9] adopted the harmonic linearization method to develop the DFIG system positive and negative sequence impedance modeling. The influence of the PI controller parameters and phase locked loop control on the impedance modeling result are analyzed, moreover the DFIG SSR under different rotor speeds are also investigated. The impedance modeling of the entire DFIG system and the series compensated weak grid network are reported in [10], with the conclusion that the interaction between the electric network and the converter controller is the main contribution of the SSR phenomena.

For the purpose of mitigating the SSR, a Thyristor-Controlled Series Capacitor (TCSC) – based method is developed [11] to flexibly adjust the impedance of the series compensated capacitance, then the potential SSR can be avoided. Similarly, the Gate-Controlled Series Capacitor (GCSC) for series compensation and SSR damping in doubly-fed induction generator (DFIG)-based wind farms is also developed in [14] to reshape the series compensated weak network. On the other hand, the impedance of DFIG system can also be reshaped in order to damp the SSR. The design of an auxiliary SSR damping controller and the selection of the control signals in the DFIG converters are explored in [13] in order effectively to mitigate the SSR. A virtual resistance is inserted to achieve damping of the DFIG SSR in [7], but yet no theoretical analysis and design procedure of this virtual resistance is reported in details.

Besides the series compensated weak network that consists of network resistance, inductance and capacitance in series connection, the parallel compensated weak network is also likely to occur, with the configuration of network resistance and inductance in series connection, while the shunt capacitance is connected in parallel [15]. In practical situation, the parallel compensated weak network occurs due to the requirement of reactive power compensation and power factor corrections. Moreover, for the case of cable-based wind power plants [16], the parasite capacitance between the cable and ground is inevitable, this also contributes to the shunt capacitance in the parallel compensated weak network.

Similar as the SSR phenomenon, when connected to the parallel compensated weak network, the DFIG system may suffer from HFR [15], naturally the impedance modeling obtained from SSR analysis in [7]-[14] can be used to analyze the HFR. Ref. [15] investigated the HFR phenomenon when the DFIG system is connected to the parallel compensated weak network. For the sake of mitigating the HFR, a virtual impedance with the combination of resonant controller and virtual positive capacitance or virtual negative inductance is introduced in either rotor current control in RSC or converter side filter current control in GSC. The impedance of DFIG system can be appropriately reshaped, i.e., the phase response can be reduced and acceptable phase margin can be achieved. Note that the HFR resonance frequency needs to be detected in [15] as an input information of the virtual impedance.

The high frequency resonance in the grid connected

The authors are with the Department of Energy Technology, Aalborg University, Aalborg 9220, Denmark. (e-mail: yis@et.aau.dk, fbl@et.aau.dk .

converter has been well analyzed before, and its active damping strategies have been well investigated in [17]-[28]. A virtual impedance across the grid-side inductance, which can be represented by a series RL branch in parallel with a negative inductance, is added through the grid current feedback control in [17]. Besides the traditional LCL filter, the active damping for the converter with series LC filter is also studied in [18]. Ref. [20]-[21] introduced a virtual RC impedance, i.e., the positive resistance to achieve better performance of harmonic resonance damping, and the negative inductance to reduce the grid side inductor for the purpose of better harmonic distortion mitigation. The grid impedance seen from the point of common coupling is reshaped in [23], thus the potential oscillations and resonance propagation in the parallel grid-connected converters can be dynamically mitigated. A cascaded adaptive notch filter structure is firstly adopted in [24] to identify the unknown resonance frequency, then an active damping can be implemented according to the detected resonance frequency. An overview of the virtual impedance based active damping strategy for the grid-connected voltage source and current source converters are summarized in [25], and several alternative methods of implementing the virtual impedance are proposed. Since the converter control parameters may influence its stability, the systematic design method of the controller parameter is given based on the chosen LCL filter resonance frequency in [26]-[27]. A capacitor current feedback active damping is achieved by shifting the capacitor current sampling instant towards the PWM reference update instant in [28], so that the reduced computation delay can be realized.

Based on the above, it is clear that the active damping strategies for the high frequency resonance in the grid connected converter can be transplanted to mitigate the HFR in the DFIG system, especially with the introduction of an appropriate virtual impedance in the resonance frequency range. In order to eliminate the influence of the proposed virtual impedance on the DFIG output average active and reactive power control, a high-pass filter is introduced in the proposed strategy, thus the virtual impedance is only effective in the high resonance frequency range. It should be pointed out that unlike the previous work [15], no HFR frequency detection unit is required in the proposed active damping strategy, thus making the proposed active damping strategy easier and simpler to implement. Besides, the resonances within certain wide frequency range can all be damped without the adjustment of virtual impedance parameters, the detailed explanations about these advantages will be given in following parts.

This paper is organized as follows: The impedance modeling of the DFIG machine and Rotor Side Converter (RSC), as well as the Grid Side Converter (GSC) and LCL filter, are first established, then the overall DFIG system impedance can be deduced as HFR analysis basis in Section II. The HFR between the DFIG system and the parallel compensated weak network (series RL + shunt C) is analyzed in Section III. The proposed active damping strategy in the DFIG stator branch with the introduction of the high-pass filter and virtual positive resistance is illustrated in details in Section IV. The parameters design of the high-pass filter cutoff frequency and the virtual positive resistance are also analyzed by the theoretical deduction. The proposed active damping strategy is validated by experimental results in Section V. Finally, the conclusions are given in Section VI.

II. DFIG System Impedance Modeling

As a basis for the following analysis, the DFIG system impedance modeling needs to be obtained. The DFIG system impedance modeling using L filter for GSC has been reported in [7]-[14], however in this paper the LCL filter is adopted due to its better switching harmonics filtering performance. Moreover, the digital control delay of 1.5 sampling period [15]-[16] caused by the voltage/current sampling and the PWM update is also taken into consideration in the impedance modeling.

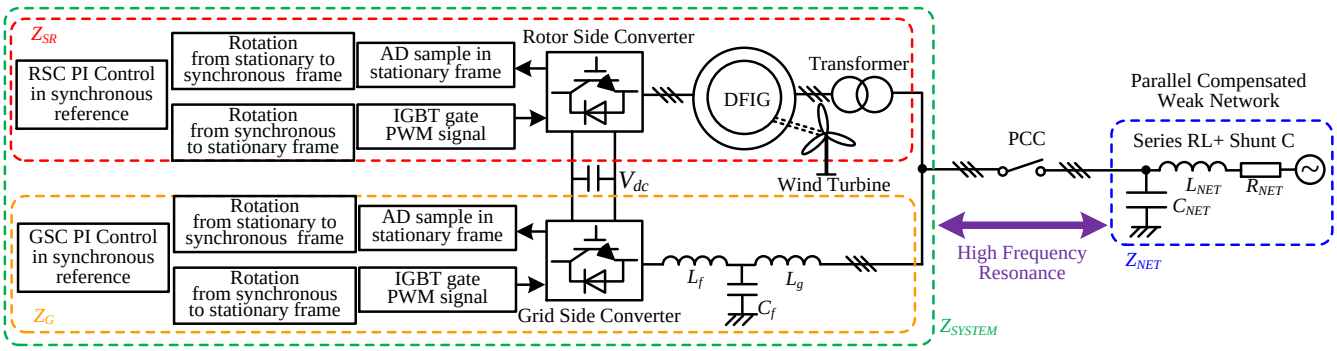

Fig. 1. Diagram of the DFIG system and the parallel compensated weak network

A. General description of the investigated DFIG system

Fig. 1 shows the diagram of the DFIG system and the parallel compensated weak grid. Since the weak network with the impedance configurations of non- compensated weak network (series RL) and the series compensated network (RLC in series) both behave as inductive units in the high frequency range, the HFR is not possible to occur due to the inductive character of the DFIG system. Thus in this paper the parallel compensated network (series RL + shunt C) is taken into consideration as the weak network

configuration.

The RSC controls the rotor voltage to deliver the DFIG machine stator output active and reactive power, the GSC provides a stable dc-link voltage. In order to prevent grid connection inrush and inner system current circulation, a transformer is connected between the DFIG stator winding and the PCC. Since the transformer does not change the voltage level of primary side and secondary side and the leakage inductance of the transformer is always small and can be regarded as part of the DFIG stator leakage inductance, the transformer will be neglected in the following discussions on the impedance modeling.

B. DFIG system impedance

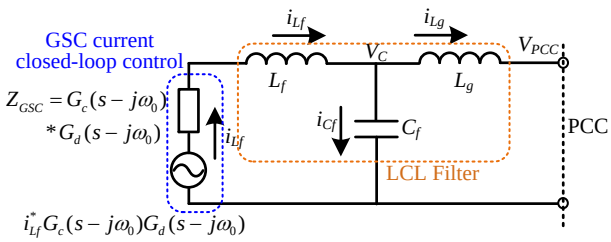

Fig. 2. Impedance modeling of the Grid Side Converter and LCL filter

The grid part of the DFIG system contains the GSC and the LCL filter, thus based on [17], the impedance modeling of the GSC and LCL filter can be presented as shown in Fig. 2. $G_c(s\text{-}j\omega_0)$ is the PI controller including the proportional part K_{pgsc} and the integral part $K_{igsc}/(s\text{-}j\omega_0)$, their parameters are available in Table I. $G_d(s\text{-}j\omega_0)$ is the digital control delay of 1.5 sampling periods. Note that ω_0 is the grid network fundamental component angular speed of 100π rad/s, it is introduced to denote the reference frame rotation from the stationary frame (where the impedance modeling is built) to the synchronous frame (where the PI closed-loop current control is implemented) as shown in Fig. 1.

Normally, the GSC control has the outer control loop of the dc-link voltage, however since the closed-loop control of dc-link voltage has relatively slow dynamic response with the control bandwidth below 100 Hz, while the high frequency resonance of DFIG system in this paper is higher than 1 kHz. Therefore, the dc-link voltage closed-loop control in GSC is neglected [10]-[13] in this paper. The grid synchronization is also neglected for the similar reasons of slow dynamic responses [10].

Thus, as shown in Fig. 2, the current closed-loop control in GSC is modeled as a voltage source $i_{Lf}^* G_c(s\text{-}j\omega_0)G_d(s\text{-}j\omega_0)$ in series connection with one impedance $Z_{GSC} = G_c(s\text{-}j\omega_0)G_d(s\text{-}j\omega_0)$.

Then the impedance of the DFIG grid part Z_G, including GSC and LCL filter, can be obtained by setting the voltage source to zero as,

$$Z_G = \frac{Z_{Cf}\left(Z_{Lf}+Z_{GSC}\right)+Z_{Lg}\left(Z_{Lf}+Z_{GSC}\right)+Z_{Cf}Z_{Lg}}{Z_{Cf}+\left(Z_{Lf}+Z_{GSC}\right)} \quad (1)$$

where, $Z_{GSC} = G_c(s\text{-}j\omega_0)G_d(s\text{-}j\omega_0)$, $Z_{Cf} = 1/sC_f$, $Z_{Lf} = sL_f$, $Z_{Lg} = sL_g$. C_f is the LCL filter capacitance, L_f is the LCL converter side inductance, L_g is the LCL grid side inductance.

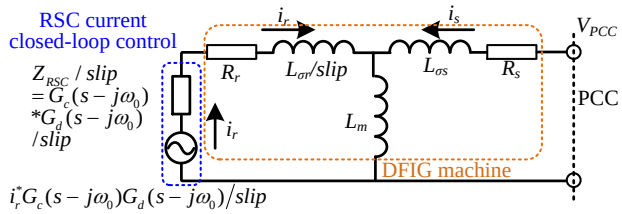

Fig. 3. Impedance modeling of the Rotor Side Converter and DFIG machine

On the other hand, based on [10], the impedance modeling of the RSC and DFIG machine can be obtained as shown in Fig. 3. The impedance of RSC and DFIG machine Z_{SR} can be obtained by setting the rotor control voltage source to zero as,

$$Z_{SR} = \frac{Z_{Lm}H+\left(R_s+Z_{L\sigma s}\right)H+Z_{Lm}\left(R_s+Z_{L\sigma s}\right)}{Z_{Lm}+H} \quad (2)$$

where $H = R_r + (Z_{L\sigma r} + Z_{RSC})/slip$; $Z_{RSC} = G_c(s\text{-}j\omega_0)G_d(s\text{-}j\omega_0)$; $Z_{Lm} = sL_m$; $Z_{L\sigma r} = sL_{\sigma r}$; $Z_{L\sigma s} = sL_{\sigma s}$. R_r is the rotor resistance, L_m is the mutual inductance, $L_{\sigma r}$ is the rotor leakage inductance, $L_{\sigma s}$ is the stator leakage inductance.

Since the rotor current control and output voltage are both generated in the rotor stationary reference frame, they need to be rotated back to the stationary frame by the slip angular speed *slip* as [7]-[9],

$$slip = \left(s - j\omega_r\right)/s \quad (3)$$

where, ω_r is the rotor speed.

As shown in Fig. 1, the RSC and DFIG machine, together with the GSC and LCL filter, are connected in parallel to the PCC. Then, the DFIG system impedance Z_{SYSTEM} can be presented based on (1) and (2) as,

$$Z_{SYSTEM} = \frac{Z_G Z_{SR}}{Z_G + Z_{SR}} \quad (4)$$

A Bode diagram of RSC and DFIG machine impedance Z_{SR}, GSC and LCL filter impedance Z_G and DFIG system impedance Z_{SYSTEM} are plotted in Fig. 4, with the parameters given in Table I.

TABLE I. PARAMETERS OF THE EXPERIMENTAL ROTOR SIDE CONVERTER, DFIG MACHINE, GRID SIDE CONVERTER AND LCL FILTER

L_g	7 mH	L_f	11 mH
C_f	6.6 uF	L_m	79.3 mH
$L_{\sigma s}$	3.44 mH	$L_{\sigma r}$	5.16 mH
R_s	0.44 Ω	R_r	0.64 Ω
K_{prsc}	8	K_{irsc}	16
K_{pgsc}	8	K_{igsc}	16
ω_r	0.8 p.u.	T_d	150 µs
Rated Power	7.5 kW	Pole Pairs	2
f_s/f_{sw}	10/5 kHz	T_s	100 µs
V_{dc}	650 V	Rotor Speed	1200 rpm (0.8 p.u.)

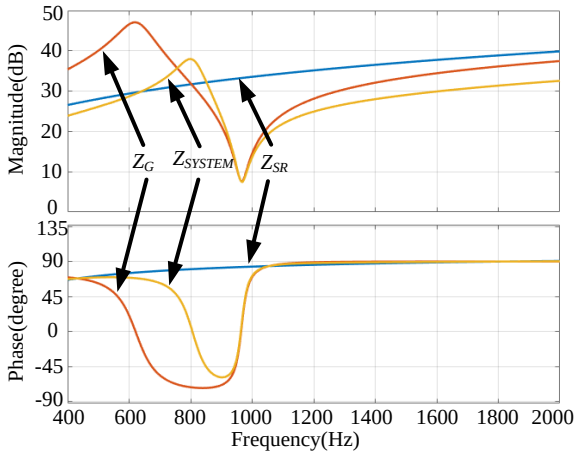

Fig. 4. Bode diagram of Rotor Side Converter and DFIG machine impedance Z_{SR}, Grid Side Converter and LCL filter impedance Z_G and DFIG system impedance Z_{SYSTEM}

As it can be observed from Fig. 4, the Z_{SR} mainly behaves as an inductive unit with a phase response about 90° at the frequency above 500 Hz. The Z_G has a magnitude peak around 620 Hz and a concave around 966 Hz caused by the LCL filter, and it has a capacitive phase response below 0° from 620 Hz and 966 Hz, which is quite opposite compared to the phase response of Z_{SR}.

The DFIG system impedance Z_{SYSTEM} has a similar magnitude and phase response as the Z_G. However, due to the involvement of Z_{SR}, the Z_{SYSTEM} magnitude peak shifts from 620 Hz to 803 Hz, and the phase response also increases in the range of 803 Hz to 966 Hz, which helps to avoid the HFR by achieving larger phase margin.

III. HFR Between DFIG System and Parallel Compensated Network

As reported in [15], a phase difference of 180° at the magnitude intersection point between the DFIG system and the weak network is the direct cause of the potential resonance. The DFIG system behaves inductive with the phase response of 90° at frequency above 1 kHz as shown in Fig. 4, thus in order to allow the HFR to happen, the weak network needs to behave capacitive with the phase response of -90° at the high frequency. Therefore, the following discussion on the HFR will be conducted on the assumption of parallel compensated weak network, i.e., series RL and shunt C network.

According to Fig. 1, the impedance of the parallel compensated weak network can be presented as,

$$Z_{NET_RL_C} = \frac{(sL_{NET} + R_{NET})/sC_{NET}}{sL_{NET} + R_{NET} + 1/sC_{NET}} \tag{5}$$

where, R_{NET} and L_{NET} are the network series resistor and inductor, C_{NET} is the network shunt capacitor.

For the sake of clearer illustration, the impedance of parallel compensated weak network can be rewritten as,

$$Z_{NET_RL_C} = \frac{s/C_{NET} + R_{NET}/L_{NET}C_{NET}}{s^2 + sR_{NET}/L_{NET} + 1/L_{NET}C_{NET}} \tag{6}$$

It can be seen from (6) that the network magnitude peak is determined by L_{NET} and C_{NET}. It is assumed that the L_{NET} remains constant, while the C_{NET} will vary according to different reactive power compensation requirements and parasite capacitance variations, thus resulting in the network impedance to shift within certain specific frequency range.

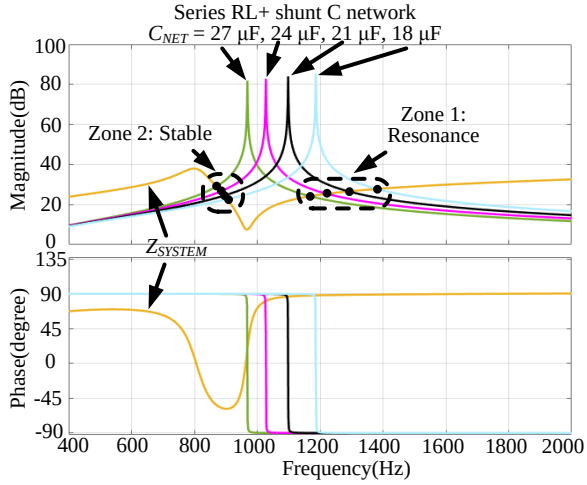

Fig. 5. Bode diagram of the DFIG system impedance and the parallel compensated weak network impedance with C_{NET} = 27 μF, 24 μF, 21 μF, 18 μF, R_{NET} = 3 mΩ, L_{NET} = 1 mH

Fig. 5 shows the Bode diagram of the DFIG system impedance and parallel compensated weak network impedance with C_{NET} = 27 μF, 24 μF, 21 μF, 18 μF respectively, R_{NET} = 3 mΩ, L_{NET} = 1 mH. Several magnitude intersection points exist in Zone 2 and Zone 1. On one hand, the intersection points in Zone 2 have the phase difference from 135° to 149°, indicating that the resonance frequency from 800 Hz to 966 Hz does not occur due to an acceptable phase margin from 31° to 45°. On the other hand, all the four intersection points in Zone 1 have phase differences of 180°, indicating that the HFR at 1160 Hz, 1220 Hz, 1290 Hz and 1380 Hz will occur respectively for the shunt capacitor C_{NET} = 27 μF, 24 μF, 21 μF, 18 μF.

Thus, it can be concluded that the HFR is very likely to happen above 1 kHz since the DFIG system impedance phase response is close to 90° at frequency above 1 kHz, while the parallel compensated network has a phase response of -90° above 1 kHz.

IV. Active Damping By High-Pass Filter and Virtual Positive Resistance

As previously analyzed, the HFR will occur as a consequence of impedance interaction between the DFIG system and the parallel compensated weak network. Effective damping of this resonance is quite critical for the DFIG system stable and reliable operation.

A. Influence of digital control delay and high-pass filter

As shown in Fig. 5, the 180° phase difference between the DFIG system and the parallel compensated weak network at the magnitude intersection frequency point is the direct reason for the HFR. Obviously, the HFR can be effectively mitigated if the phase difference at the

magnitude intersection point can be reduced and an acceptable phase margin can be achieved.

Since the DFIG system behaves as an inductive unit with phase response of 90° at the resonance frequency range, the insertion of a capacitive unit can be helpful to reduce its phase response, thus mitigate the resonance as a result.

Moreover, the digital control delay is inevitable in the DFIG system as presented in (7), as a result the originally introduced virtual positive resistance can be transformed to the combination of positive resistance and positive capacitance when considering the digital control delay as shown in Fig. 6.

$$G_d(s) = e^{-sT_d} \tag{7}$$

where, the digital control delay T_d is caused by AD sampling and PWM update. In the previous works [15]-[25], the delay caused by AD sampling is half sampling period $0.5T_s$ (T_s is the sampling period, and can be calculated based on the sampling frequency f_s as $T_s = 1/f_s$, f_s is shown in Table I as 10 kHz), and the delay caused by PWM update is one sampling period T_s, so the total delay T_d is one and half sampling period $T_d = 1.5T_s = 150$ µs.

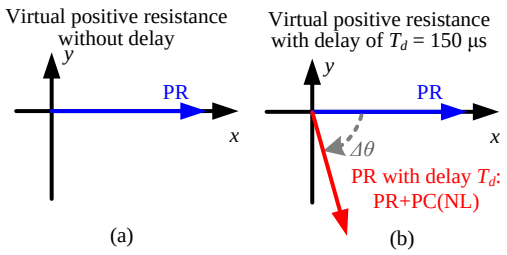

Fig. 6. Vector diagram of virtual positive resistance without / with digital control delay of T_d = 150 µs

According to Fig. 6, the inevitable digital control delay T_d = 150 µs causes a phase angle delay $\Delta\theta$, which can be calculated based on (7) as,

$$\Delta\theta = -2\pi f T_d \tag{8}$$

Based on (8), it can be found out that the phase angle delay $\Delta\theta$ varies from -54° at 1000 Hz to -108° at 2000 Hz. This means the phase delay $\Delta\theta$ caused by the inevitable digital control delay T_d is helpful by producing Positive Capacitance (PC in Fig. 6(b)) on the basis of the originally introduced virtual Positive Resistance (PR in Fig. 6(a)), thus the DFIG system phase response can be reduced.

However, the introduction of the control delay based virtual positive resistance will influence the entire frequency range, and the rotor current fundamental component control will be unfavorably affected. Thus in order to avoid the influence of virtual positive resistance at low frequency, a high-pass filter needs to be introduced as,

$$G_{hp}(s) = \frac{s}{s + 2\pi f_{cut}} \tag{9}$$

where, f_{cut} is the cutoff frequency of the high-pass filter, the design of f_{cut} will be discussed in the following part.

Fig. 7 shows the Bode diagram of the high-pass filter, with a cutoff frequency f_{cut} = 200 Hz. Clearly, the high-pass filter is able to produce a zero gain for the dc component. Thus the influence of virtual positive resistance on the rotor current error fundamental component can be eliminated. Note that due to the numerical accuracy limitation in MATLAB Bode command, only -60 dB is shown in Fig. 7, but actually the dc component can be much more significantly damped to zero according to (9).

Besides, the high-pass filter has a leading phase response, which can be calculated based on (9) as,

$$\angle G_{hp}(j\omega) = \arctan\left(\omega_{cut}/\omega\right) \tag{10}$$

The phase leading results can be seen from Fig. 7, i.e., 11.3° at 1000 Hz, 9.46° at 1200 Hz, 8.13° at 1400 Hz, 7.12° at 1600 Hz.

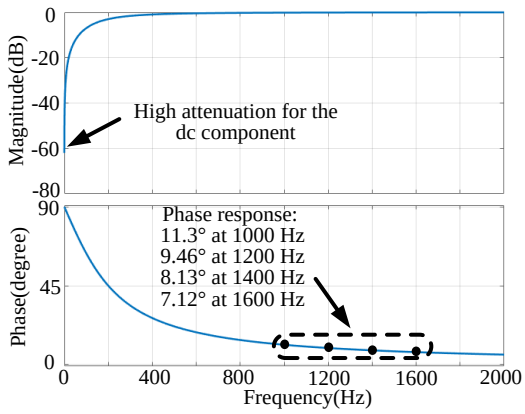

Fig. 7. Bode diagram of high-pass filter with cutoff frequency f_{cut} = 200 Hz

Then, based on (7) and (9), the virtual impedance Z_v including the virtual positive resistance, the high-pass filter, as well as the digital control delay, can be presented as,

$$Z_v(s) = R_v \frac{s}{s + 2\pi f_{cut}} e^{-sT_d} \tag{11}$$

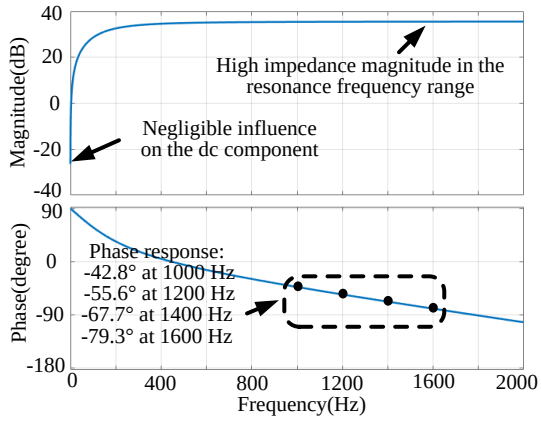

Fig. 8. Bode diagram of the virtual impedance including the virtual positive resistance R_v = 60 Ω and the high-pass filter cutoff frequency f_{cut} = 200 Hz, with control delay of T_d = 150 µs

Fig. 8 shows the Bode diagram of the virtual impedance including the virtual positive resistance R_v = 60 Ω and the high-pass filter cutoff frequency f_{cut} = 200 Hz, with control delay of T_d = 150 µs. As it can be seen, due to the adoption of a high-pass filter, the influence on the dc component can

be neglected, while a high impedance magnitude in the resonance frequency range can be obtained, which helps to damp the resonance. Besides, the phase responses are -42.8° at 1000 Hz, -55.6° at 1200 Hz, -67.7° at 1400 Hz, -79.3° at 1600 Hz. This phase response means that the virtual impedance behaves as the combination of positive resistance (helpful to increase the DFIG system resistance) and positive capacitance (helpful to reduce the DFIG system phase response).

B. Implementation of virtual impedance in the stator branch

Once the virtual impedance expression is deduced in (11), it is also important to implement this virtual impedance in the DFIG system. In this paper, based on Fig. 3, the virtual impedance is inserted to the DFIG machine stator branch as shown in Fig. 9. The introduction of virtual impedance can be regarded as a stator current feedforward control.

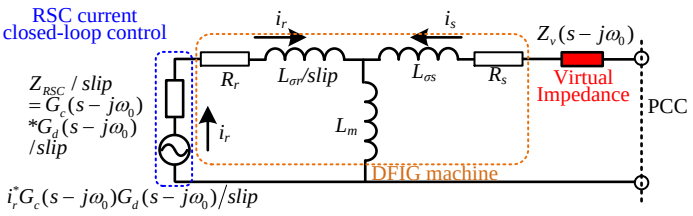

Fig. 9. Impedance modeling of RSC and DFIG machine with the introduction of virtual impedance in DFIG stator current feedforward control

Obviously, the DFIG and RSC impedance Z_{SR}^{ad}, as well as the DFIG system impedance Z_{SYSTEM}^{ad}, with the virtual impedance Z_v can be presented,

$$Z_{SR}^{ad} = \frac{Z_{Lm}H + \left(R_s + Z_{L\sigma s} + Z_v\right)H + Z_{Lm}\left(R_s + Z_{L\sigma s} + Z_v\right)}{Z_{Lm} + H} \tag{12a}$$

$$Z_{SYSTEM}^{ad} = \frac{Z_G Z_{SR}^{ad}}{Z_G + Z_{SR}^{ad}} \tag{12b}$$

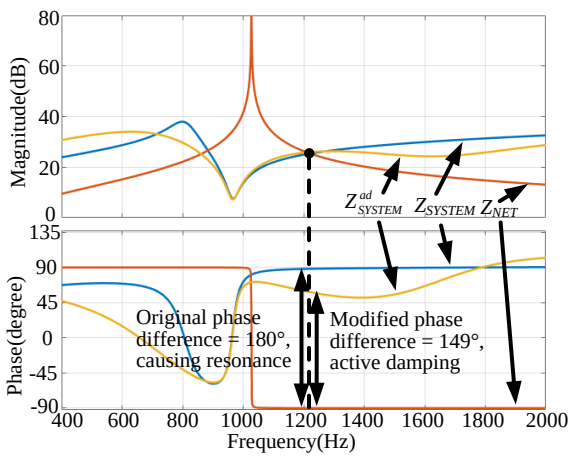

Fig. 10. Bode diagram of the DFIG system impedance and series RL + shunt C network impedance C_{NET} = 24 μF, when virtual impedance in (11) is introduced

Fig. 10 shows the Bode diagram of DFIG system impedance, when the virtual impedance in (11) is introduced. Before the virtual impedance is employed, the phase difference between the DFIG system and the weak network at about 1200 Hz is 180°, thus causing a resonance. Once the virtual impedance is introduced, due to the large virtual positive capacitance illustrated in Fig. 6 and Fig. 8, the phase response of DFIG system can be effectively reduced to 59° at 1200 Hz, and the phase difference becomes 149°, thus the resonance can be effectively mitigated.

As it can be clearly seen, the phase response of DFIG system with a virtual impedance Z_{SYSTEM}^{ad} can be reduced by more than 25° from 1100 Hz to 1600 Hz. This indicates that the potential HFRs from 1100 Hz to 1600 Hz can all be effectively damped due to the acceptable phase margin.

In conclusion, there are two advantages of the proposed active damping control strategy: 1) no resonance frequency detection unit is required. Thus the control complexity can be reduced; 2) once the virtual impedance parameters are chosen as in Fig. 8, i.e., virtual positive resistance R_v = 60 Ω and the high-pass filter cutoff frequency f_{cut} = 200 Hz, with control delay of T_d = 150 μs, the HFR resonance frequency within 1100 Hz to 1600 Hz can all be effectively mitigated due to sufficient large phase margin as shown in Fig. 10. As a result, even the weak network parameters may often deviate in practical situation and cause the HFR resonance frequency to shift within small range, the proposed active damping strategy is still capable of mitigating these resonances and proves its strong robustness against weak network parameters deviation as a result. These two advantages make the proposed active damping strategy more robust and practical in the real-world applications as well as reduce the control complexity.

Moreover, it should be pointed out that, since the virtual impedance introduced in the stator current through effective control in RSC is capable of reshaping the DFIG system impedance appropriately, it is unnecessary and even makes the control strategy unfavorably complicated if the virtual impedance is also introduce in GSC, or even in RSC and GSC simultaneously. Therefore, the virtual impedance is only introduced in RSC here, but not in GSC.

C. Virtual impedance parameters design

According to the previous analysis, the virtual impedance parameters need to be carefully designed in order to achieve an appropriate phase response decreasing in the resonance frequency range. This part discusses the parameters design of the virtual resistance R_v and high-pass filter cutoff frequency f_{cut} in (11).

1) Design of high-pass filter cutoff frequency f_{cut}

As it can be observed from (8), the phase delay caused by the digital control delay becomes larger when the frequency increases. Moreover, according to Fig. 7, the phase leading caused by the high-pass filter decreases when the frequency increases. Therefore, it can be found that the overall phase delay of the virtual impedance in Fig. 8 becomes larger as the frequency increases, which is helpful to the active damping. Based on this knowledge, the design of high-pass

filter cutoff frequency f_{cut} will be conducted for the lowest potential resonance frequency of 1000 Hz.

According to (8), the digital control delay causes phase delay of -54° at 1000 Hz, since the overall virtual impedance phase response should be chosen as at least -45° at 1000 Hz (the virtual positive capacitance has the same amplitude as the virtual positive resistance when the phase response = -45°), thus the phase leading of high-pass filter should be around 10°.

Based on (10) and the expected phase response of 10°, the appropriate cutoff frequency of the high-pass filter can be calculated as,

$$f_{cut} = f_{reso}\tan(10°) = 176\ \text{Hz} \tag{13}$$

Here, for the sake of simplicity, the high-pass cutoff frequency is chosen as f_{cut} = 200 Hz. As proved in Fig. 8, the 200 Hz cutoff frequency ensures the overall virtual impedance phase response of -42.8° at 1000 Hz, and this phase delay becomes larger as the frequency increases, which is helpful to decrease the DFIG system phase response.

2) Design of virtual resistance R_v

According to Fig. 9, the comparatively much larger mutual inductance branch in DFIG machine can be neglected [10]. The only inductive components in the DFIG machine impedance modeling are the stator leakage inductance and rotor leakage inductance.

Therefore, in order to effectively reduce the overall DFIG system phase response, the amplitude of the virtual positive capacitance in Fig. 6(b) should be as large as possible, but can not be larger than the stator leakage inductance and rotor leakage inductance, otherwise the RSC and DFIG machine would behave as a capacitive unit. Then, the following can be deduced,

$$-R_v\sin(\theta) < 2\pi f_{reso}\left(L_{\sigma s} + L_{\sigma r}\right) \tag{14a}$$

$$\theta = \arctan\left(f_{cut}/f_{reso}\right) - 2\pi f_{reso}T_d \tag{14b}$$

where, θ is the phase response of virtual impedance shown in Fig. 8. By substituting θ = -42.8°, f_{reso} = 1000 Hz, $L_{\sigma s}$ = 3.44 mH and $L_{\sigma r}$ = 5.16 mH into (14), the virtual resistance R_v should be smaller than 79.5 Ω, from a conservation point of view, the R_v is chosen 60 Ω as shown in Fig. 8. Note that the parameter R_v is also partly determined by f_{cut}. Thus R_v needs to be adjusted if the cutoff frequency f_{cut} varies.

Based on the above design analysis of high-pass filter cutoff frequency f_{cut} and virtual resistance R_v, it can be found that it is easy to determine these parameters, that is, the variation of f_{cut} will change the effective active damping range, while the adjustment of R_v can vary the phase margin at the resonance frequency.

D. Control block diagram

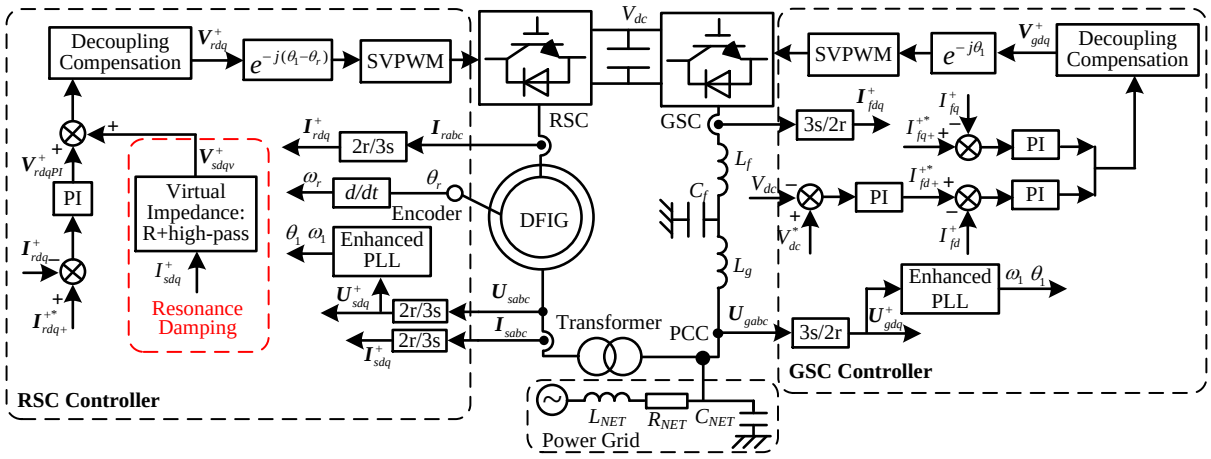

Fig. 11. Control block diagram of the DFIG system HFR active damping strategy through virtual impedance: positive resistance and high-pass filter.

Fig. 11 shows the control block diagram of the proposed active damping strategy implemented through stator current feedforward control in the RSC. As it can be seen, for the RSC control, an Enhanced Phase Locked Loop (EPLL) [3]-[4] is able to provide the information of grid voltage fundamental synchronous angular speed ω_1 and angle θ_1 information, while an encoder gives out the DFIG rotor position θ_r and speed ω_r. The rotor current $\boldsymbol{I}^+_{rdq}$ is first sampled and then controlled based on the reference value $\boldsymbol{I}^{+*}_{rdq}$ with a PI controller to output the harvested wind energy. The stator current $\boldsymbol{I}^+_{sdq}$ is also sampled for the feedforward control with the introduction of virtual impedance. Note that no resonance frequency detection unit is necessary in the proposed control strategy, thus the control complexity can be reduced.

The output of the rotor current PI closed-loop control $\boldsymbol{V}^+_{rdqPI}$ and the output of virtual impedance resonance damping $\boldsymbol{V}^+_{sdqv}$, are added, together with the decoupling compensation, giving out the rotor control voltage $\boldsymbol{V}^+_{rdq}$, which is then transformed to the rotor stationary frame and delivered as the input to the Space Vector Pulse Width Modulation (SVPWM).

As for the GSC control, the dc-link voltage V_{dc} is well regulated by a PI controller, and its output is delivered as the converter side inductance filter current reference $\boldsymbol{I}^{+*}_{fdq}$, which is used to regulate the actual converter side inductance filter current $\boldsymbol{I}^+_{fdq}$ by a PI controller. Similarly, the GSC control voltage $\boldsymbol{V}^+_{gdq}$ can be obtained by the PI current controller output and the decoupling compensation unit.

V. Experimental Validation

A. Experimental setup

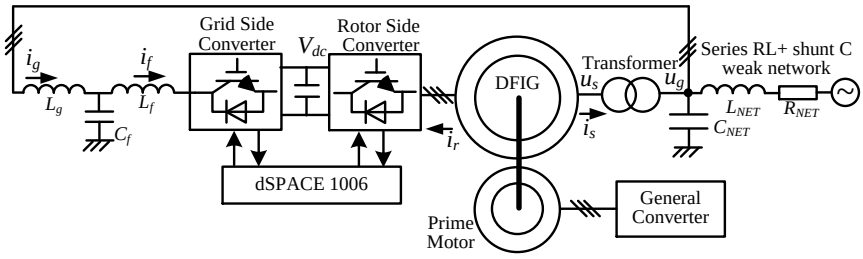

Fig. 12. Setup of 7.5 kW DFIG system test rig

In order to experimentally validate the correctness of the proposed active damping strategy for the DFIG system HFR, a down-scaled 7.5 kW test rig is built up as shown in Fig. 12. The experimental DFIG system parameters can be found in Table I. The weak network is simulated using three phase inductors and capacitors. The DFIG is externally driven by a prime motor, and two 5.5 kW Danfoss motor drives are used for the GSC and the RSC, both of them are controlled with dSPACE 1006. The rotor speed is set to 1200 rpm (0.8 p.u.), with the synchronous speed of 1500 rpm (1.0 p.u.). The dc-link voltage is 650 V. The switching frequency f_{sw} for both RSC and GSC is 5 kHz, the sampling frequency f_s for both RSC and GSC is 10 kHz. The voltage level of the DFIG system is 400 V.

The experimental validation is conducted under weak network parameters of R_{NET} = 3 mΩ, L_{NET} = 1.5 mH, C_{NET} =10 μF. According to (13) and (14), during the experimental validation, the cutoff frequency f_{cut} is chosen to 300 Hz and the virtual resistance is chosen to 70 Ω due to the resonance frequency of 1600 Hz in the experimental results.

B. *Experimental results*

Fig. 13 shows the experimental result of the steady state response of DFIG system when active damping control strategy is disabled under sub-synchronous speed of 1200 rpm (0.8 p.u.). Due to the above analyzed impedance interaction between the DFIG system and the parallel compensated weak network grid, three phase stator voltage u_s and current i_s, rotor current i_r, grid side voltage u_g and current i_g contains the HFR around 1600 Hz.

Fig. 14 shows the steady state response of the DFIG system when the active damping strategy is enabled at the sub-synchronous speed of 1200 rpm. Obviously, the HFR in Fig. 13 can be effectively mitigated when the active damping strategy is enabled, and as a result the resonance components in the stator voltage and current, grid side voltage and current becomes much smaller. Therefore, the effectiveness of the proposed active damping strategy under sub-synchronous speed can be validated.

Fig. 15 shows the dynamic response of the DFIG system when the active damping strategy is enabled at sub-synchronous speed of 1200 rpm. Once enabled, the active damping strategy is capable of mitigating the HFR components within 10 ms in the stator voltage and current, as well as the grid side voltage and current. This experimental result verifies a good dynamic performance of the proposed active damping strategy in practical applications.

Similar to the experimental results under sub-synchronous speed, the experimental results under super-synchronous speed are also provided as shown in Figs. 16 - 18. Fig. 16 shows the steady state response of the DFIG system when the active damping strategy is disabled at super-synchronous speed of 1700 rpm (1.13 p.u.). The HFR of 1600 Hz also occurs in the case of Fig. 13. This experimental result verifies that the rotor speed has negligible influence on the resonance frequency. Fig. 17 shows the steady state response of DFIG system at super- synchronous speed when the active damping strategy is enabled. Similar satisfactory active damping performance can be achieved as in the case of Fig. 14. Fig. 18 shows the dynamic response of the DFIG system at the instant of enabling the active damping strategy at super-synchronous speed of 1700 rpm (1.13 p.u.). The fast dynamic response time of around 10 ms can also be achieved, which is beneficial to the damping of the HFR.

Therefore, the experimental results are able to validate the effectiveness of the proposed active damping control strategy for the DFIG system HFR from the perspective of both steady state and dynamic response, and under both sub- and super- synchronous speed conditions.

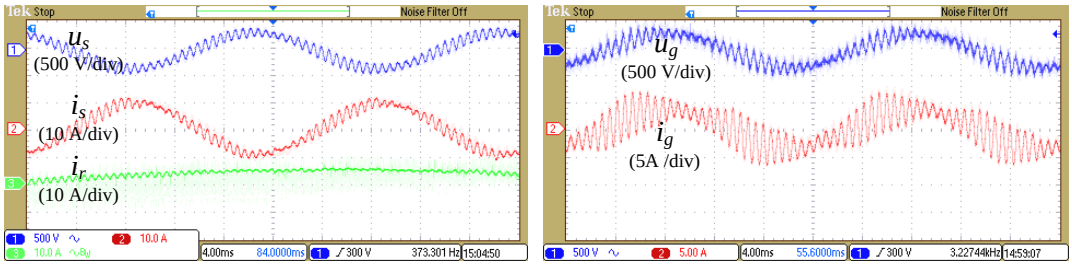

Fig. 13. Steady state response of DFIG system when active damping strategy is disabled, at sub-synchronous speed of 1200 rpm (0.8 p.u.)

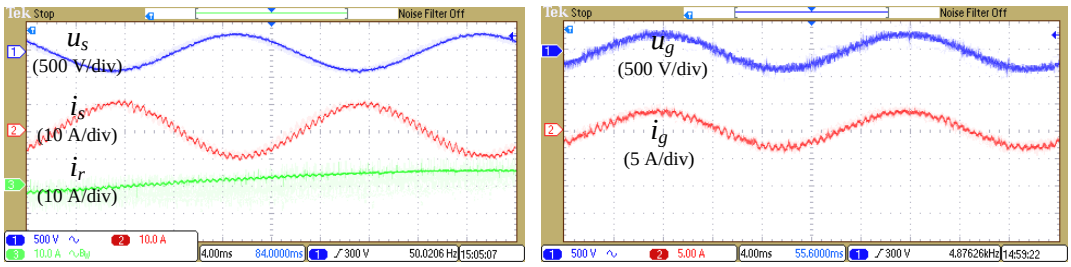

Fig. 14. Steady state response of DFIG system when active damping strategy is enabled, at sub-synchronous speed of 1200 rpm (0.8 p.u.)

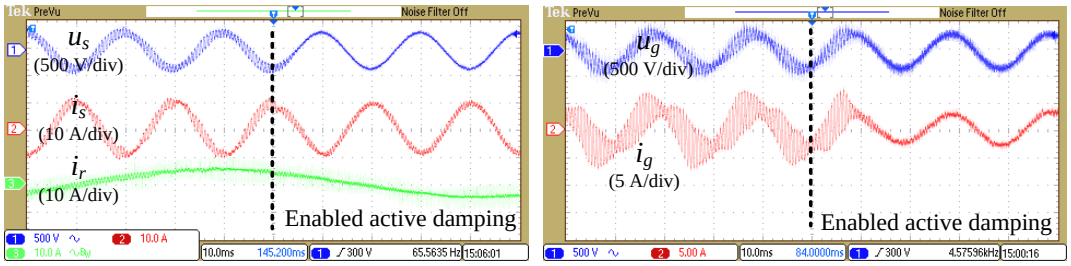

Fig. 15. Dynamic response of DFIG system when active damping strategy is enabled, at sub-synchronous speed of 1200 rpm (0.8 p.u.)

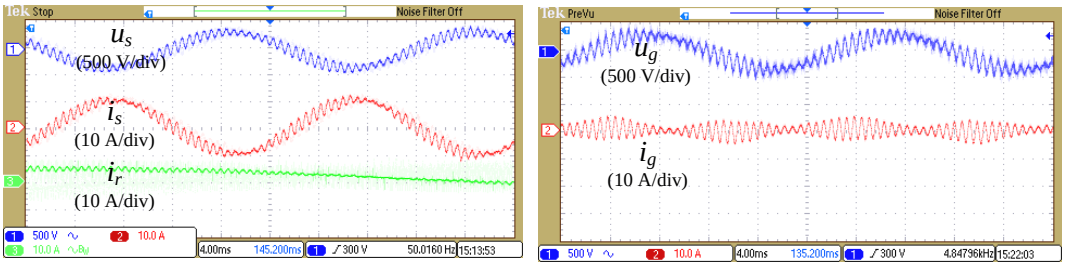

Fig. 16. Steady state response of DFIG system when active damping strategy is disabled, at super-synchronous speed of 1700 rpm (1.13 p.u.)

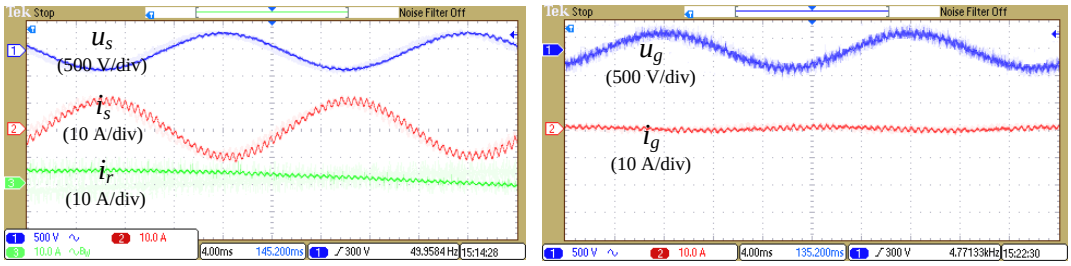

Fig. 17. Steady state response of DFIG system when active damping strategy is enabled, at super-synchronous speed of 1700 rpm (1.13 p.u.)

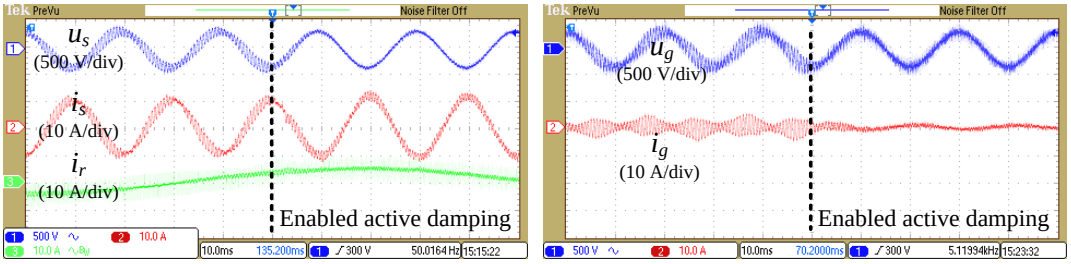

Fig. 18. Dynamic response of DFIG system when active damping strategy is enabled, at super-synchronous speed of 1700 rpm (1.13 p.u.)

VI. Conclusion

This paper has investigated a wide frequency band active damping control strategy for DFIG system under parallel compensated weak network. Following conclusions can be drawn,

1) The HFR can be analyzed and estimated based on the impedance modeling of the DFIG system and the parallel compensated weak network.
2) The active damping is achieved with the implementation of virtual resistance and high-pass filter in DFIG stator current feedforward control with the consideration of the digital control delay. No resonance frequency detection is needed, and wide frequency band resonances can all be mitigated with unchanged virtual impedance parameters.
3) The parameter design of the virtual resistance and high-pass filter cutoff frequency are theoretically analyzed and obtained, and larger high-pass filter cutoff frequency indicates higher active damping frequency range, while larger virtual resistance indicates larger phase margin.

References

[1] F. Blaabjerg, and K. Ma, "Future on Power Electronics for Wind Turbine Systems," *IEEE J. Emer. Sel. Topics Power Electron.*, vol. 1, no. 3, pp. 139-152, Sep. 2013.

[2] H. Nian, P. Cheng, and Z. Q. Zhu, "Coordinated Direct Power Control of DFIG System Without Phase-Locked Loop Under Unbalanced Grid Voltage Conditions," *IEEE Trans. Power Electron.*, vol. 31, no. 4, pp. 2905 - 2918, Apr. 2016.

[3] Y. Song, H. Nian, "Modularized Control Strategy and Performance Analysis of DFIG System Under Unbalanced and Harmonic Grid Voltage," *IEEE Trans. Power Electron.*, vol. 30, no. 9, pp. 4831 - 4842, Sept. 2015.

[4] H. Nian, Y. Song, “Direct Power Control of Doubly Fed Induction Generator Under Distorted Grid Voltage,” *IEEE Trans. Power Electron.*, vol. 29, no. 2, pp. 894-905, Feb. 2014.

[5] R. Zhu, Z. Chen, Y. Tang, F. Deng, and X Wu, “Dual-Loop Control Strategy for DFIG-Based Wind Turbines Under Grid Voltage Disturbances,” *IEEE Trans. Power Electron*., vol. 31, no. 3, pp. 2239 - 2253, Mar. 2016.

[6] W. Chen, F. Blaabjerg, N. Zhu, M. Chen, and D. Xu, “Doubly Fed Induction Generator Wind Turbine Systems Subject to Recurring Symmetrical Grid Faults,” *IEEE Trans. Power Electron*., vol. 31, no. 2, pp. 1143 - 1160, Feb. 2016.

[7] I. Vieto, and J. Sun, “Damping of Subsynchronous Resonance Involving Type-III Wind Turbines,” *in Proc. Control and Modeling for Power Electronics* (COMPEL), pp. 1-8, 2015.

[8] I. Vieto, and J. Sun, “Small-Signal Impedance Modeling of Type-III Wind Turbine,” *in Proc. Power & Energy Society General Meeting* (PESG), pp. 1-5, 2015.

[9] I. Vieto, and J. Sun, “Real-time Simulation of Subsynchronous Resonance in Type-III Wind Turbines,” *in Proc. Control and Modeling for Power Electronics* (COMPEL), pp. 1-8, 2014

[10] Z. Miao, “Impedance-Model-Based SSR Analysis for Type 3 Wind Generator and Series-Compensated Network,” *IEEE Trans. Energy Convers.*, vol. 27, no. 4, pp. 984–991, Dec. 2012.

[11] L. Piyasinghe, Z. Miao, J. Khazaei, and L. Fan, “Impedance Model-Based SSR Analysis for TCSC Compensated Type-3 Wind Energy Delivery Systems,” *IEEE Trans. Sustainable Energy.*, vol. 6, no. 1, pp. 179–187, Jan. 2015.

[12] L. Fan, and Z. Miao, “Nyquist-Stability-Criterion-Based SSR Explanation for Type-3 Wind Generators,” *IEEE Trans. Energy Convers.*, vol. 27, no. 3, pp. 807–809, Sep. 2012.

[13] L. Fan, and Z. Miao, “Mitigating SSR Using DFIG-Based Wind Generation,” *IEEE Trans. Sustainable Energy.*, vol. 3, no. 3, pp. 349–358, July 2012.

[14] H. A. Mohammadpour and E. Santi, "Modeling and Control of Gate-Controlled Series Capacitor Interfaced With a DFIG-Based Wind Farm," *IEEE Trans. Ind. Electron*., vol. 62, no. 2, pp. 1022-1033, Feb. 2015.

[15] Y. Song, X. Wang, and F. Blaabjerg, “High Frequency Resonance Damping of DFIG based Wind Power System under Weak Network,” *IEEE Trans. Power Electron*., vol. PP, no. 99, early access.

[16] X. Wang, F. Blaabjerg, and P. C. Loh, “Proportional derivative based stabilizing control of paralleled grid converters with cables in renewable power plants,” *in Proc. Energy Conversion Congress and Exposition* (ECCE), pp. 4917 - 4924, 2014.

[17] X. Wang, F. Blaabjerg, and P. C. Loh, “Grid-Current-Feedback Active Damping for LCL Resonance in Grid-Connected Voltage Source Converters,” *IEEE Trans. Power Electron*., vol. 31, no. 1, pp. 213-223, Jan. 2016.

[18] X. Wang, Y. Pang, P. C. Loh, and F. Blaabjerg, “A Series-LC-Filtered Active Damper With Grid Disturbance Rejection for AC Power-Electronics-Based Power Systems,” *IEEE Trans. Power Electron*., vol. 30, no. 8, pp. 4037-4041, Aug. 2015.

[19] X. Wang, F. Blaabjerg, and P. C. Loh, “Virtual RC Damping of LCL-Filtered Voltage Source Converters With Extended Selective Harmonic Compensation,” *IEEE Trans. Power Electron*., vol. 30, no. 9, pp. 4726-4737, Sep. 2015.

[20] X. Wang, F. Blaabjerg, and Z. Chen, “Synthesis of Variable Harmonic Impedance in Inverter-Interfaced Distributed Generation Unit for Harmonic Damping Throughout a Distribution Network,” *IEEE Trans. Ind. Appl*., vol. 48, no. 4, pp. 1407-1417, July-Aug. 2012.

[21] X. Wang, F. Blaabjerg, and Z. Chen, “Autonomous Control of Inverter Interfaced Distributed Generation Units for Harmonic Current Filtering and Resonance Damping in An Islanded Microgrid,” *IEEE Trans. Ind. Appl*., vol. 50, no. 1, pp. 452-461, Jan.-Feb. 2014.

[22] X. Wang, F. Blaabjerg, and W. Wu, “Modeling and Analysis of Harmonic Stability in an AC Power-Electronics-Based Power System,” *IEEE Trans. Power Electron.*, vol. 29, no. 12, pp. 6421-6432, Dec. 2014.

[23] X. Wang, F. Blaabjerg, M. Liserre, Z. Chen, J. He, and Y. Li, “An Active Damper for Stabilizing Power-Electronics-Based AC Systems,” *IEEE Trans. Power Electron*., vol. 29, no. 7, pp. 3318-3329, July 2014.

[24] X. Wang, F. Blaabjerg, and M. Liserre, “An Active Damper to Suppress Multiple Resonances with Unknown Frequencies,” *in Proc. Applied Power Electronics Conference and Exposition* (APEC), pp. 2184-2194, 2014.

[25] X. Wang, Y. Li, F. Blaabjerg, and P. C. Loh, “Virtual-Impedance-Based Control for Voltage-Source and Current-Source Converters,” *IEEE Trans. Power Electron*., vol. 30, no. 12, pp. 7019-7037, Dec. 2015.

[26] C. Bao, X. Ruan, X. Wang, W. Li, D. Pan, and K. Weng, “Step-by-Step Controller Design for LCL-Type Grid-Connected Inverter with Capacitor–Current-Feedback Active-Damping,” *IEEE Trans. Power Electron*., vol. 29, no. 3, pp. 1239-1253, Mar. 2014.

[27] D. Pan, X. Ruan, C. Bao, W. Li, and X. Wang, “Optimized Controller Design for LCL-Type Grid-Connected Inverter to Achieve High Robustness Against Grid-Impedance Variation,” *IEEE Trans. Ind. Electron*., vol. 62, no. 3, pp. 1537-1547, Mar. 2015.

[28] D. Pan, X. Ruan, C. Bao, W. Li, and X. Wang, “Capacitor-Current-Feedback Active Damping With Reduced Computation Delay for Improving Robustness of LCL-Type Grid-Connected Inverter,” *IEEE Trans. Power Electron*., vol. 29, no. 7, pp. 3414-3427, July 2014.

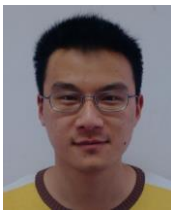

Yipeng Song (S’14–M’16) was born in Hangzhou, China. He received the B.Sc. degree and Ph.D. degree both from the College of Electrical Engineering, Zhejiang University, Hangzhou, China, in 2010 and 2015. He is currently working as a Postdoc at the Department of Energy Technology in Aalborg University, Denmark. His current research interests are motor control with power electronics devices in renewable-energy conversion, particularly the control and operation of doubly fed induction generators for wind power generation.

Frede Blaabjerg (S’86–M’88–SM’97–F’03) was with ABB-Scandia, Randers, Denmark, from 1987 to 1988. From 1988 to 1992, he was a Ph.D. Student with Aalborg University, Aalborg, Denmark. He became an Assistant Professor in 1992, Associate Professor in 1996, and Full Professor of power electronics and drives in 1998. His current research interests include power electronics and its applications such as in wind turbines, PV systems, reliability, harmonics and adjustable speed drives.

He has received 17 IEEE Prize Paper Awards, the IEEE PELS Distinguished Service Award in 2009, the EPE-PEMC Council Award in 2010, the IEEE William E. Newell Power Electronics Award 2014 and the Villum Kann Rasmussen Research Award 2014. He was an Editor-in-Chief of the IEEE TRANSACTIONS ON POWER ELECTRONICS from 2006 to 2012. He is nominated in 2014 and 2015 by Thomson Reuters to be between the most 250 cited researchers in Engineering in the world.